國立臺灣大學工學院材料科學與工程學系

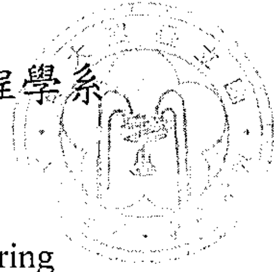

博士論文

Department of Materials Science and Engineering

College of Engineering

National Taiwan University

Doctoral Dissertation

探索無外加磁場自旋軌道矩機制以實現高效能磁性與類神經形態記憶體系統

Exploring Field-Free Spin-Orbit Torque Mechanisms for High-Efficiency Magnetic and Neuromorphic Memory Systems

林俊逸

Chun-Yi Lin

指導教授：白奇峰 博士

Advisor: Chi-Feng Pai, Ph.D.

中華民國 115 年 4 月

April, 2026

doi:10.6342/NTU202600984

口試委員會審定書

國立臺灣大學博士學位論文
口試委員會審定書

DOCTORAL DISSERTATION ACCEPTANCE CERTIFICATE
NATIONAL TAIWAN UNIVERSITY

(論文中文題目)
(Chinese title of Doctor's Thesis)
探索無外加磁場自旋軌道矩機制以實現高效能磁性與類神經形態記憶體系統

(論文英文題目)
(English title of Doctor's Thesis)
Exploring Field-Free Spin-Orbit Torque Mechanisms for High-Efficiency Magnetic and Neuromorphic Memory Systems.

本論文係 林俊逸 D10527001 在國立臺灣大學 材料科學與工程學系 完成之博士學位論文，於民國 114 年 6 月 3 承下列考試委員審查通過及口試及格，特此證明。

The undersigned, appointed by the Department / Graduate Institute of Materials Science and Engineering on 3 June 2025, have examined a Doctoral Dissertation entitled above presented by **Chun-Yi Lin** D10527001 candidate and hereby certify that it is worthy of acceptance.

口試委員
Oral examination committee:

白奇峰 (指導教授 Advisor)

莊子弘

宋明遠

楊朝堯

Luqiao Liu

系(所、學位學程)主管 Director: 蔡豐羽

doi:10.6342/NTU202600984

謝誌

在學士逕讀博士班的過程中，老實說一路以來非常匆忙。像是在追趕著什麼，卻又常感到力有未逮，轉眼間就到了離開的時候。所幸途中遇到許多貴人相助，也一直提醒自己要付出相對應的努力，盡力完成這份研究論文以及博士學位。

首先，我想感謝我的指導教授：白奇峰博士。跟白老師對話就像是看見一片大海般的寬廣，是我第一次感受到知識的浩瀚，。謝謝白老師打造很好的研究環境，也非常感謝老師的信任，讓我能夠盡情探索不同的可能性：包括在臺積電實習、參加 MIT 的訪問計畫，以及在實驗室進行各種題目與想法的嘗試，每一個階段都受益匪淺。

謝謝在同輻時莊博的指導，以及魏博的「Aim high, never settle down.」，讓我感受到對學術的熱忱，也成為我選擇逕讀博士班的初衷。

剛進入實驗室時，感謝彭成瑋學長手把手帶我學會基本磁性量測與製程，以及陳天玥學長指導。也感謝實驗室的博士班學長：胡宸瑜、劉彥廷、黃宇豪、佳晉、兆中作為我的榜樣。當然，還要感謝廖唯邦學長，過去兩年中，他在實驗和心態上給了我許多寶貴的建議，對我幫助良多。

博二進入了臺積電研發部門實習，最感謝宋明遠博士，他就像百科全書一般，跟我分享像是 P-bit、domain wall logic 的知識。感謝元浚和 EDM 團隊的同事們，讓我學習如何成為一個兼具深度與廣度的博士生。也很榮幸自己可以見證 SOT-MRAM 在業界研發的歷程。

做學長後，很感謝柏筌、子晏、子騫、席維、老黎、Ponnie 一起為實驗室努力，也謝謝子權、瑞旭的幫忙。謝謝我材料系的朋友們：摯文、軒翊、羽皓，還有很多人，包含系辦人員的協助。

在 MIT 生活中感謝在這邊的朋友們邀約一起吃飯，也很開心靠打排球認識很多很棒的人。謝謝劉魯喬老師願意給我這個機會，Josh 跟秋原都是很棒的學習目標，跟他們說話就像在跟兩個教授討論知識，也很榮幸跟由夫以及 Tudor 一起學習。

doi:10.6342/NTU202600984

在臺大做實驗到半夜遇到白鼻心；在 MIT 燒壞幾十顆 MTJ 的夜晚遇到浣熊。雖然這五年仍然有美中不足，我想也已經盡力了。

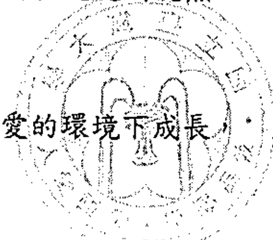

最後，我要謝謝我的家人：爸爸、媽媽跟姊姊，讓我在充滿愛的環境下成長，我一直努力希望能成為你們的驕傲。

本論文獲財團法人國防工業發展基金會獎學金與台積電博士獎學金贊助。

doi:10.6342/NTU202600984

摘要

在人工智慧(AI)時代，次世代記憶體技術受到高度關注，需具備節能、高密度以及可類比編程等特性，以支援大規模神經形態運算。自旋軌道矩(SOT)裝置因具有非揮發性、高耐久性與互補式金屬氧化物半導體(CMOS)製程相容性而備受關注，更重要的是，它能透過磁區壁運動等穩定且可控制的物理機制，實現可靠的類比切換行為。此一穩定性優於其他次世代記憶體技術，如電阻式記憶體(RRAM)與相變記憶體(PCM)，使自旋軌道矩裝置特別適合用於多位元突觸權重的實現。

本論文研究三種不需外加磁場的自旋軌道矩切換機制：包括尼爾橘皮效應、膜層間 Dzyaloshinskii-Moriya 交互作用以及傾斜磁異向性。這些機制皆透過微米尺寸的霍爾量測元件進行實驗，並以鎢(W)與鉑(Pt)為基底材料進行異質結構製作。為系統化比較各裝置表現，本研究建立統一的評估架構，涵蓋切換效率、熱穩定性、可分辨的電阻狀態數與週期間變異性等關鍵指標。

在所有測試裝置中，傾斜磁異向性樣品展現最佳的類比行為，能穩定實現 11 個量化的電阻狀態，且週期間變異性低於 3%，有助於實現穩定的多位元權重表示。進一步引入銥錳反鐵磁層(IrMn)可提升熱穩定性，但會降低類比切換能力。為了與類比設計進行比較與互補，本研究亦展示一種數位型自旋突觸，透過將四個二進位的自旋軌道轉矩記憶體元件組合成一個突觸，實現 2 位元權重解析度與更高的操作穩定性。

本研究進一步將微米尺寸霍爾元件的量測特性投射至實際的自旋軌道轉矩記憶體(SOT-MRAM)架構中，以進行系統層級的效能評估。使用 NeuroSim 模擬平台，在 32 奈米製程節點下，針對類比型與數位型自旋軌道轉矩記憶體，以及傳統靜態隨機存取記憶體（SRAM）進行電路層級模擬與比較。結果顯示，數位型設計於 MNIST 手寫辨識資料集上可達 92.2% 的推論準確率，且讀取能耗與延遲皆低於靜態隨機存取記憶體；類比型設計則展現出更優異的能源效率，但為達成相似的推論準確率，仍需克服隧道磁阻比不足的挑戰。

doi:10.6342/NTU202600984

本論文建立一套完整的無外場自旋軌道矩裝置之實驗與建模分析框架，並針對材料設計、裝置架構與電路整合提出關鍵見解，希冀有助於未來自旋記憶體與神經形態運算系統的發展與應用。

關鍵詞：自旋電子學、零外場自旋軌道轉矩切換、類比自旋電子突觸、神經形態運算。

doi:10.6342/NTU202600984

ABSTRACT

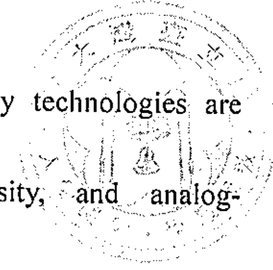

In the era of artificial intelligence (AI), emerging memory technologies are increasingly expected to provide energy-efficient, high-density, and analog-programmable capabilities to support large-scale neuromorphic computing. Spin-orbit torque (SOT) devices stand out not only for their non-volatility, high endurance, and complementary metal-oxide-semiconductor (CMOS) compatibility, but more importantly, for their ability to robustly realize analog switching behaviors through physical mechanisms such as domain wall propagation. This level of stability exceeds that of other emerging memories such as resistive random access memory (RRAM) and phase change memory (PCM), making SOT devices particularly suitable for implementing multi-level synaptic weights in neuromorphic architectures.

This dissertation investigates three field-free current-induced SOT switching mechanisms: the Néel orange-peel effect, interlayer Dzyaloshinskii-Moriya interaction (i-DMI), and tilted magnetic anisotropy. These mechanisms are experimentally studied using micron-scale Hall bar devices fabricated from W- and Pt-based heterostructures. A unified benchmarking framework is developed to quantify switching efficiency, thermal stability, analog programmability, and cycle-to-cycle (CTC) variation.

Among the evaluated devices, the tilted anisotropy sample demonstrates the best analog behavior, achieving 11 clearly separated resistance states with less than 3% CTC variation. This supports stable multi-level weight representation for neuromorphic

doi:10.6342/NTU202600984

computing. The introduction of an IrMn antiferromagnetic layer further improves thermal stability but limits analog switching. A digital spintronic synapse is also demonstrated by grouping four binary SOT device cells to achieve 2-bit resolution and enhanced robustness to complement analog designs.

The measured characteristics from micron-scale Hall bar devices are projected onto practical SOT- magnetic random access memory (MRAM) architectures to enable system-level evaluation. Subsequently, device-to-circuit simulations are performed using NeuroSim at the 32 nm technology node to benchmark analog SOT-MRAM, digital SOT-MRAM, and SRAM. Digital SOT-MRAM achieves 92.2% inference accuracy on the MNIST dataset, with lower read energy and latency than SRAM. The analog design shows comparable energy-delay benefits but requires a higher ON/OFF ratio to reach similar accuracy.

This work establishes a comprehensive experimental and modeling framework for field-free SOT devices and provides insights into material engineering, device architecture, and circuit-level integration for future spintronic memory and neuromorphic systems.

Keywords: Spintronics, field-free spin-orbit torque (SOT) switching, analog spintronic synapse, neuromorphic computing.

doi:10.6342/NTU202600984

CONTENTS

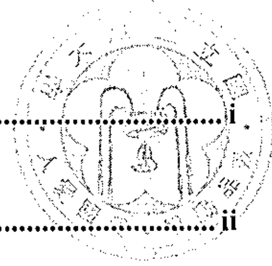

口試委員會審定書 i

謝誌 ii

摘要 iv

ABSTRACT vi

CONTENTS viii

LIST OF FIGURES x

LIST OF TABLES xviii

Chapter 1 Introduction 1

1.1 Background and motivation 1

1.2 The opportunities and drawbacks of emerging memory 3

1.3 The importance of field-free solution in type-z SOT devices 5

1.4 Scope and organization of this dissertation 9

Chapter 2 Experimental Method 11

2.1 Overview of magnetron sputtering 11

2.2 Columnar growth and wedge geometry 14

2.3 Substrate rotation and deposition uniformity 18

2.4 Effect of sputtering power on film characteristics 20

doi:10.6342/NTU202600984

2.5 Working pressure and scattering dynamics 21

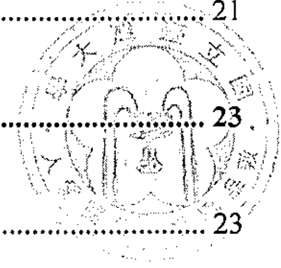

Chapter 3 W-based field-free solutions **23**

3.1 Néel orange-peel effect 23

Chapter 4 Pt-based field-free solutions **32**

4.1 I-DMI effect 32

4.2 Tilted anisotropy effect 43

4.3 Tilted anisotropy effect with IrMn 50

Chapter 5 Analog SOT devices for neural network applications **57**

Chapter 6 Digital SOT devices for neural network applications **73**

Chapter 7 Summary and Outlook **82**

PUBLICATIONS **85**

Bibliography **88**

doi:10.6342/NTU202600984

LIST OF FIGURES

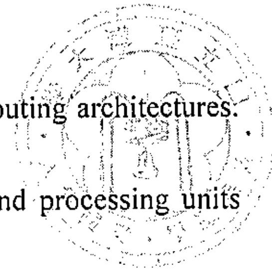

Fig. 1.1 Challenges of Modern AI workloads on conventional computing architectures. (a) Von Neumann architecture, where separate memory and processing units communicate via a shared bus. (b) Number of model parameters in representative deep learning architectures over time[3]. 3

Fig. 1.2 Current-induced domain wall dynamics. (a) Schematic illustration of domain wall motion in a magnetic structure of PMA without H_x. (b) Schematic illustration of domain wall propagation in a magnetic structure of PMA under H_x[28]. 8

Fig. 2.1 Schematic of a basic sputter deposition system with a single vacuum chamber with one sputter source[58]. 12

Fig. 2.2 Magnetron sputtering. (a) Schematic illustration of the magnetron sputtering process[58]. (b) Photograph of a used 2-inch target, showing a distinct ring-shaped erosion area where material has been consumed 14

Fig. 2.3 Cross-sectional STEM analysis of Nb(8)/Ta(70) heterostructure. (a) Low-magnification overview showing the full stack, including the Si wafer, SiO_2 layer, sputtered thin film, and the protective top layer. (b) High-magnification STEM image with colored outlines highlighting individual columnar grains. (c) FFT patterns extracted from selected grains confirm their crystalline structure and alignment with the underlying seed layer, indicating columnar growth during the sputtering process. 17

doi:10.6342/NTU202600984

Fig. 3.1 Device structure and measurement configuration for the Néel orange-peel effect. (a) Schematic illustration of a CoFeB/W/CoFeB/MgO/Ta multilayer stack. (b) The Hall bar device and the coordinate system for electrical measurements. 24

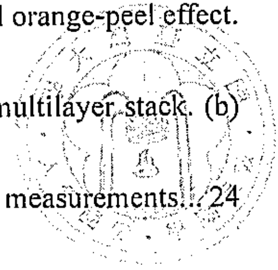

Fig. 3.2 The hysteresis loop shift measurement on the Néel orange-peel effect sample (Sample I). (a) The field-swept AHE hysteresis loop. (b) Representative shifted loops under $I_{DC} = \pm 6.5$ mA without any in-plane field. (c) The switching fields of down-to-up (DN-to-UP, red triangles), up-to-down (UP-to-DN, blue squares) transitions, and H_z^{eff} (black circles) as functions of I_{DC}. (d) The field-free current-induced magnetization switching loop. 26

Fig. 3.3 Roughness engineering and current-induced effective field optimization. (a) Schematic illustration of two different deposition modes with 0 RPM and 30 RPM of the sample holder rotation speed. (b) RMS roughness of the CoFeB(4)/W(1.4) surface under different rotation speeds, extracted from AFM measurements. (c) Field-free current-induced magnetization switching loops for samples processed at 10 RPM and 30 RPM. (d) H_z^{eff}/I_{DC} as a function of RMS roughness. The dashed line indicates the field-saturated $H_z^{eff}/I_{DC} = 3.7$ Oe/mA. 28

Fig. 3.4 W thickness dependence of field-free switching. (a) M_r/M_s and H_c as functions of t_W. (b) Field-free current-induced switching ratio as a function of t_W. 30

doi:10.6342/NTU202600984

Fig. 3.5 The thermal stability of Sample I. (a) Representative current-induced switching loops with t_{pulse} = 500 ms and 10 ms. (b) J_c as a function of the applied current pulse width.......... 31

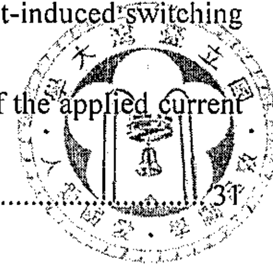

Fig. 4.1 Schematic illustration of the Ta/CoFeB/Pt/Co/Pt multilayer stack.......... 33

Fig. 4.2 Characterization of i-DMI in Ta(0.5)/CoFeB(1.4)/Pt(3.3)/Co(0.7)/Pt(t) heterostructures. (a) The upper illustration shows the structures of the layer stacks and the relationship between the Pt deposition direction and the D direction. The lower shows the coordinate system of the experiment and the corresponding Hall bar device for electrical measurements. (b) Representative shifted OOP hysteresis loops under H_{φ} = 300 Oe with φ_H = 90° and 270°. (c) H_{offset} as a function of φ_H. The blue squares and red circles represent data from t = 0.6 nm (asymmetric) and 3.3 nm (symmetric) designs. (d) H_{DMI} as a function of capping Pt thickness. The solid line represents a fit based on Bruno's model for interlayer exchange coupling.......... 36

Fig. 4.3 The hysteresis loop shift measurement on the i-DMI sample (Sample II). (a) The field-swept AHE hysteresis loop. (b) Representative shifted loops under I_{DC} = ±2.5 mA without any in-plane field. (c) The switching fields of down-to-up (red triangles), up-to-down (blue squares) transitions, and H_z^{eff} (black circles) as functions of I_{DC}. (d) The field-free current-induced magnetization switching loop. 38

doi:10.6342/NTU202600984

Fig. 4.4 AHE measurements during (a) z-field scanning and (b) y-field scanning. 39

Fig. 4.5 The i-DMI characterization on samples with various oblique deposition recipes. (a) The OOP AHE hysteresis loops of different film growth conditions. (b) H_{offset} as functions of φ_H. 40

Fig. 4.6 The i-DMI and VSM measurements on samples with two different Pt capping layer thicknesses (t = 0.8 nm vs. t = 1 nm). (a) H_{offset} as a function of φ_H. (b) OOP VSM data of the samples. 42

Fig. 4.7 The thermal stability of Sample II. (a) Representative current-induced switching loops with different current pulse widths. (b) J_c as a function of the applied current pulse width. 43

Fig. 4.8 Spacer Pt thickness dependence of i-DMI. (a) H_c and H_{DMI} as functions of t_{Pt}. (b) J_c as a function of the spacer Pt thickness. The sign corresponds to the switching current of the DN-to-UP transition. (c) and (d) The current-induced magnetization switching loops of CoFeB/Pt(3.3)/Co/Pt and CoFeB/Pt(5.3)/Co/Pt at 50 ms pulse. 45

Fig. 4.9 Schematic illustration of the Ta/Pt/Co/Pt multilayer stack. 46

Fig. 4.10 The hysteresis loop shift measurement on the tilted anisotropy sample (Sample III). (a) The field-swept AHE hysteresis loop. (b) Representative shifted loops under I_{DC} = ±6.5 mA without any in-plane field. (c) The switching fields of down-to-up (red triangles), up-to-down (blue squares) transitions, and H_z^{eff}

doi:10.6342/NTU202600984

(black circles) as functions of I_{DC}. (d) The field-free current-induced magnetization switching loop. 47

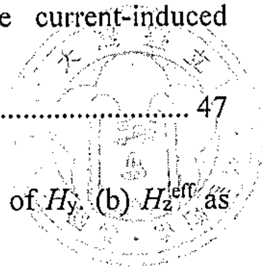

Fig. 4.11 Tilted anisotropy vs. i-DMI sample. (a) H_{offset} as functions of H_y. (b) H_z^{eff} as functions of I_{DC}. 49

Fig. 4.12 The thermal stability of Sample III. (a) Representative current-induced switching loops with different current pulse widths. (b) J_c as a function of the applied current pulse width. 50

Fig. 4.13 EB in Ta/Pt/Co/Pt/IrMn/Ta heterostructures. (a) Schematic illustration of the layer structure. (b) AHE hysteresis loop of the Ta/Pt/Co/Pt/IrMn/Ta stack. (c) H_c and H_{ex} as functions of the IrMn sputtering power. (d) The XRD pattern comparison of samples deposited at different sputtering powers. 52

Fig. 4.14 Field-free current-induced EB switching enabled by tilted anisotropy in the Ta/Pt/Co/Pt/IrMn/Ta structure. (a) Schematic of the heterostructure, highlighting the oblique deposition of the bottom Pt layer. (b), (c) Current-induced EB switching measured under $H_x = 0$ and –300 Oe, respectively. (d) Switching phase diagram of the tilted anisotropy device. (e) The pole figure of the IrMn(111) texture for the control sample with fully rotated deposition. (f) The pole figure of the IrMn(111) texture for the sample with a wedged bottom Pt layer. 55

doi:10.6342/NTU202600984

Fig. 4.15 The thermal stability of Sample IV. (a) Representative current-induced switching loops with different current pulse widths. (b) J_c as a function of the applied current pulse width. 56

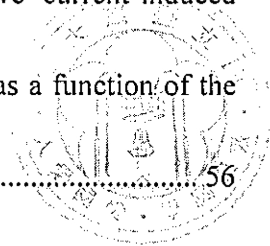

Fig. 5.1 Memristive behaviors in the tilted anisotropy device (Sample III) with sequential 50 μs current pulses. (a) The upper panel shows the Hall bar device and coordinate system for electrical measurements. The lower panel demonstrates current-induced magnetization switching under a current pulse of 50 μs. (b) The first train of current pulses, consisting of 19 identical positive pulses at I_{pulse} = 13 mA, applied after a large reset pulse of I_{reset} = -23.5 mA, and (c) the corresponding R_H response. (d) The second train of current pulses, consisting of 19 identical I_{pulse} = -13 mA, applied after a large reset pulse of I_{reset} = 23.5 mA, and (e) the corresponding R_H response. 60

Fig. 5.2 Demonstration of 11 distinguishable resistance states in the tilted anisotropy device (Sample III) using sequential 50 μs current pulses. (a) and (d) Applied pulse trains composed of 6 predefined pulse counts (referred to as sequences) and an I_{reset}. (b) and (e) Corresponding R_H responses for each sequence. (c) Seven distinguishable states obtained from the first pulse train (down-to-up switching). (f) Additional states obtained from the second pulse train (up-to-down switching). (g) The CDFs of R_H, showing 11 clearly distinguishable resistance states across both switching directions. 64

doi:10.6342/NTU202600984

Fig. 5.3 Demonstration of distinguishable resistance states in Sample I (a) Current-induced magnetization switching under a current pulse of 50 ms. (b) The corresponding response of R_H, where equal 49 positive I_{pulse} of 3.1 mA are applied after a large I_{reset} of -6 mA. (c) The response of R_H corresponds to 3 specific magnetic states. (d) The CDFs vs. R_H for 3 distinguishable states. 66

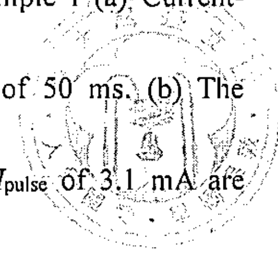

Fig. 5.4 Demonstration of distinguishable resistance states in Sample II (a) Current-induced magnetization switching under a current pulse of 10 μs. (b) The corresponding response of R_H, where equal 9 I_{pulse} of 3.5 mA are applied after a large I_{reset} of -6 mA. (c) The response of R_H corresponds to 4 specific current pulse numbers. (d) The CDFs vs. R_H for 4 distinguishable states. 67

Fig. 5.5 Demonstration of distinguishable resistance states in Sample IV (a) Current-induced magnetization switching under t_{pulse} = 50 μs. (b) The corresponding response of R_H, where equal 19 I_{pulse} of different amplitudes are applied after a large I_{reset} of -40 mA. 72

Fig. 6.1 Architectures of synaptic cores for neuromorphic hardware accelerators[5].... 74

Fig. 6.2 Demonstration of quantized synaptic response using a quad-channel Hall bar device. (a) Schematic illustration of a quad-channel Hall bar structure with four separate input current paths (I_1 to I_4), enabling independent control of each magnetic element for discrete weight representation. (b) Comparison between the R_H output of a single Hall cross and a quad-channel Hall bar under current

doi:10.6342/NTU202600984

pulse sweeping. (c) Measured LTP and LTD characteristics of the quad-channel device, achieved by selectively aligning the magnetic states of individual channels. 76

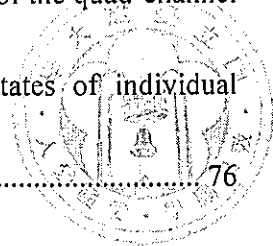

Fig. 6.3 System-level evaluation of digital and analog SOT synapse implementations. (a) Circuit schematic of a single-cell analog SOT-MRAM device with a 2T1R configuration. (b) Circuit schematic of a digital SOT-MRAM synapse composed of four binary cells (N = 4) to represent 2-bit weights. (c) Schematic of the two-layer MLP neural network architecture used for NeuroSim simulations, consisting of 400 input neurons, 100 hidden neurons, and 10 output neurons for MNIST digit recognition. (d) Inference accuracy as a function of the conductance ON/OFF ratio 79

doi:10.6342/NTU202600984

LIST OF TABLES

Table 1. The benchmark table of three field-free solutions for neuromorphic computing. 70

Table 2. The benchmark table for different types of memories........ 81

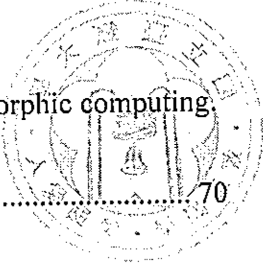

doi:10.6342/NTU202600984